Durham University

Durham Research Online

Deposited in DRO:

22 February 2016

Version of attached file:

Accepted Version

Peer-review status of attached file:

Peer-reviewed

Citation for published item:

Coombs, W.M. and Petit, O.A. and Ghaffari Motlagh, Y. (2016) 'NURBS plasticity : yield surface representation and implicit stress integration for isotropic inelasticity.', Computer methods in applied mechanics and engineering., 304 . pp. 342-358.

Further information on publisher's website:

http://dx.doi.org/10.1016/j.cma.2016.02.025

Publisher's copyright statement:

© 2016 This manuscript version is made available under the CC-BY-NC-ND 4.0 license
http://creativecommons.org/licenses/by-nc-nd/4.0/

Additional information:

Use policy

The full-text may be used and/or reproduced, and given to third parties in any format or medium, without prior permission or charge, for personal research or study, educational, or not-for-profit purposes provided that:

- a full bibliographic reference is made to the original source
- a link is made to the metadata record in DRO
- the full-text is not changed in any way

The full-text must not be sold in any format or medium without the formal permission of the copyright holders.

Please consult the full DRO policy for further details.

Durham University Library, Stockton Road, Durham DH1 3LY, United Kingdom
Tel : +44 (0)191 334 3042 | Fax : +44 (0)191 334 2971
https://dro.dur.ac.uk

NURBS plasticity: yield surface representation and implicit stress integration for isotropic inelasticity

William M. Coombs[a], Oscar A. Petit[b], Yousef Ghaffari Motlagh[a]

[a] *School of Engineering and Computing Sciences, Durham University*
Science Site, South Road, Durham, DH1 3LE, UK.
T: +44 (0) 191 334 2516, F: +44 (0) 191 334 2408, E: w.m.coombs@durham.ac.uk
[b] *AECOM, First Floor, 1 Trinity Gardens, Newcastle upon Tyne, NE1 2HF, UK*

Abstract

In numerical analysis the failure of engineering materials is controlled through specifying yield envelopes (or surfaces) that bound the allowable stress in the material. However, each surface is distinct and requires a specific equation describing the shape of the surface to be formulated in each case. These equations impact on the numerical implementation, specifically relating to stress integration, of the models and therefore a separate algorithm must be constructed for each model. This paper presents, for the first time, a way to construct yield surfaces using techniques from non-uniform rational basis spline (NURBS) surfaces, such that any isotropic convex yield envelope can be represented within the same framework. These surfaces are combined with an implicit backward-Euler-type stress integration algorithm to provide a flexible numerical framework for computational plasticity. The algorithm is inherently stable as the iterative process starts and remains on the yield surface throughout the stress integration. The performance of the algorithm is explored using both material point investigations and boundary value analyses demonstrating that the framework can be applied to a variety of plasticity models.

Keywords:
elasto-plasticity, constitutive modelling, non-uniform rational basis spline (NURBS), stress integration, finite element analysis

1. Introduction

Constitutive models provide stress versus strain relationships for different engineering materials and are at the heart of any numerical boundary value simulation method (such as the finite element method). The majority of boundary value solvers are strain-driven in that they require a model to return an updated stress state given a previous stress state and a strain increment. However, constitutive models are typically constructed in rate form and therefore a stress integration algorithm is required to perform this process.

There is a vast array of constitutive models available in literature and the library of available models is continually expanding. It is therefore not possible to provide a comprehensive review of all of these models within this paper. Instead focus is placed on general classes on stress integration techniques used to implement these models. For a more general review of constitutive modelling for various materials see Yu [40], see the work of Simo and Hughes [29] regarding their numerical implementation and specifically focused on their implementation within the finite element method see the work of Kojić [15].

The numerical implementation of constitutive models can be broadly split into three categories: (i) explicit, (ii) implicit and (iii) exact stress integration methods. Explicit methods stem from the work of Ilyushin's [13] method of successive elastic solutions and was subsequently applied to the Prandtl-Reuss constitutive model (von Mises yield surface with linear isotropic elasticity) by Mendelson [21]. Nayak and Zienkiewicz [24] were the first to formulate a general explicit stress integration procedure for use within the finite element method and several models have been subsequently implemented using their method. However, the major drawback of these methods is that they do not enforce the consistency condition at the end of the stress-strain path [37].

Implicit stress integration methods were first proposed by Wilkins [39] who used a radial return method for a Prandtl-Reuss model. Implicit techniques use a predictor-corrector methodology where the problem is split into an elastic prediction followed by a (typically, iterative) plastic correction for states that violate the yield criteria. See [9, 29] for a detailed review of implicit methods for computational plasticity. Several other implicit stress integration procedures have been proposed over the last 50 years, including [14–16, 25, 30], in addition to some analytical integration methods [6, 7, 10]. The major advantage of these implicit approaches is that the consistency conditions are enforced at the updated stress state. However, they are computationally more complex compared to explicit methods and require derivatives of both the flow rule and the hardening laws that can become involved for advanced models.

Exact stress integration is only possible for a small sub-set of plasticity models, such as the widely used Prandtl-Reuss and Drucker-Prager models, for example (see the works of [17–20, 35, 38]). Although these models provide useful benchmarks for other approximate methods they are generally considered to be too computationally expensive for general use in finite element analyses [20]. However, computational efficiency aside, the major drawback of these approaches is the bespoke algorithm required in each case and the limited number of models that these techniques can be applied to.

Several papers have compared explicit and implicit approaches to stress integration including [1, 19, 27], amongst others. Implicit methods have some significant advantages over, simpler, explicit methods in that they: allow for larger strain increments to be applied, rigorously enforce the consistency conditions (see Section 2.1) and allow the derivation of the algorithmic consistent tangent [22, 32] that facilitates optimum convergence of the boundary value simulation.

In the vast majority of constitutive models the failure is controlled through specifying yield envelopes (or surfaces) that bound the allowable stress in the material. Simple examples include the prismatic von Mises (circle) and Tresca (hexagon) yield surfaces. However, each surface is distinct and requires a specific equation describing the shape of the surface to be formulated in each case. This yield equation impacts on the stress integration and therefore a specific algorithm must be constructed for each model. The approach followed in this paper is to construct a yield envelope using a non-uniform rational basis spline (NURBS) surface and combining this with an implicit stress integration algorithm such that any isotropic convex yield surface can be described and integrated using the same numerical framework.

Due to the geometric nature of the method presented in this manuscript, the majority of the paper is presented in principal stress and strain space with the following ordering of the principal stresses

$$\sigma_1 \geq \sigma_2 \geq \sigma_3,$$

with tensile stresses taken as positive. Note that although the equations are presented in principal stress space we can do this without loss of generality of the final result as the principal quantities are simply transferred back to generalised quantities at the end of the algorithm. Generalised, 6-component, stress and strain quantities are denoted using $\hat{(\cdot)}$. The paper also uses a mixture of tensor and matrix notation with the use of matrices restricted to aspects relating to numerical implementation.

The layout of the paper is as follows: Section 2 details a plasticity theory based on yield envelopes constructed from NURBS surfaces, Section 3 provides the numerical implementation of this theory including an implicit stress integration algorithm and consistent tangent, Section 4 provide numerical examples both at a material point level and within boundary value finite element analyses, conclusions are drawn in Section 5.

2. NURBS plasticity

This section provides the essential equations required to define a NURBS surface and include it within a plasticity framework. For more detailed information on the construction of NURBS-based surfaces see the work of Piegl and Wayne [26].

A NURBS surface can be expressed as

$$S_k(\xi, \eta) = \sum_{i=0}^{n} \sum_{j=0}^{m} R_{i,j}(\xi, \eta)(C_k)_{i,j}, \tag{1}$$

where k is the physical index and the NURBS basis functions are give by

$$R_{i,j}(\xi,\eta) = \frac{N_{i,p}(\xi)N_{j,q}(\eta)w_{i,j}}{\sum_{k=0}^{n}\sum_{l=0}^{m} N_{k,p}(\xi)N_{l,q}(\eta)w_{k,l}} \tag{2}$$

and C_k are the control point positions, $N_{i,p}$ and $N_{j,q}$ are the p^{th} and q^{th}-degree B-spline basis functions (see [8, 26], amongst others), ξ and η are the local positions within the two Knot vectors that describe the surface and $w_{i,j}$ are the weights associated with the control points.

2.1. NURBS-based yield envelopes

Starting from the equation for a NURBS surface (1), a NURBS-based yield envelope can be expressed as

$$f = \Big(\sigma_i - S_i(\xi,\eta)\Big)(S_{,\sigma})_i = 0, \tag{3}$$

where $(S_{,\sigma})_i$ is the surface outward normal and σ_i the principal stress state (that is, the partial derivative of S with respect to stress). The yield surface separates stress space into two regions: an elastic region where $f < 0$ and an inadmissible region where $f > 0$. The boundary between these two regions ($f = 0$) is used to define material failure and points on this surface will undergo elasto-plastic deformation. The outward normal to the yield envelope can be obtained through the cross product of the two local derivatives

$$(S_{,\sigma})_i = (S_{,\eta} \times S_{,\xi})_i = \epsilon_{ijk}(S_{,\eta})_j(S_{,\xi})_k, \tag{4}$$

where ϵ_{ijk} is the Levi-Civita tensor[1]. See [26] for efficient algorithms for the calculation of the derivatives of the NURBS surface with respect to the local coordinates. For associated flow plasticity theory the outward normal to the yield surface also provides the flow direction, that is

$$\dot{\varepsilon}_i^{\mathrm{p}} = \dot{\gamma}(S_{,\sigma})_i, \tag{5}$$

where $\dot{\gamma}$ is the scalar plastic multiplier (or consistency parameter). This plastic multiplier must satisfy the Kuhn-Tucker-Karush consistency conditions

$$f(\sigma_i) \leq 0, \qquad \dot{\gamma} \geq 0 \qquad \text{and} \qquad f(\sigma_i)\dot{\gamma} = 0. \tag{6}$$

These conditions enforce that the material must either be on the yield surface undergoing elasto-plastic deformation ($f = 0$ and $\dot{\gamma} \geq 0$) or inside the yield surface with purely elastic behaviour ($f \leq 0$ and $\dot{\gamma} = 0$).

[1] $\epsilon_{ijk} = 0$ if $i = j$, $j = k$ or $k = i$, $\epsilon_{ijk} = 1$ for even permutations of i, j and k and $\epsilon_{ijk} = -1$ for odd permutations of i, j and k.

2.2. Stress integration

The central problem in computational plasticity is; given a previously converged elastic strain state, $(\varepsilon^{\mathrm{e}}_n)_i$ (or equivalently a converged stress state, σ^n_i), that is subjected to a strain increment, $\Delta\varepsilon_i$, what is the updated elastic strain state, $(\varepsilon^{\mathrm{e}}_{n+1})_i$? The strain increment comes from the boundary value simulation under consideration. The problem stems from the fact that inelastic constitutive relationships are constructed in rate form and must be integrated to create such an incremental relationship.

In this paper we consider an implicit elastic predictor, plastic corrector scheme. Within this framework the elastic trial strain is given by

$$\sigma^t_i = \sigma^n_i + \Delta\sigma_i, \qquad \text{where} \qquad \Delta\sigma_i = D^{\mathrm{e}}_{ij}\Delta\varepsilon_j \qquad \text{and} \qquad \sigma^n_i = D^{\mathrm{e}}_{ij}(\varepsilon^{\mathrm{e}}_n)_j. \tag{7}$$

σ^n_i is the stress state from the previous load (or time) step in the global solution algorithm, $\Delta\varepsilon_i$ is the strain increment from associated with the global boundary value displacement and D^{e}_{ij} contains the principal components of the linear elastic stiffness matrix.

If the trial elastic stress state exceeds the yield envelope ($f > 0$) then it must be corrected back onto the yield surface using a plastic stress increment

$$\sigma^r_i = \sigma^t_i - \Delta\sigma^{\mathrm{p}}_i, \qquad \text{where} \qquad \Delta\sigma^{\mathrm{p}}_i = D^{\mathrm{e}}_{ij}\Delta\varepsilon^{\mathrm{p}}_j \tag{8}$$

and $\Delta\epsilon^{\mathrm{p}}_j$ is the plastic strain increment obtained from the incremental form of (5). Once this correction has been applied the updated elastic strain can be obtained from

$$(\varepsilon^{\mathrm{e}}_{n+1})_i = (\varepsilon^{\mathrm{e}}_n)_i + \Delta\varepsilon_i - \Delta\varepsilon^{\mathrm{p}}_i. \tag{9}$$

The next section adopts a closest point projection (CPP) implicit stress integration algorithm to arrive at the updated stress, and strain, state.

2.3. CPP & energy mapped stress space

Simo and Hughes [29] showed that the backward Euler (bE) integration corresponds to the minimisation of

$$\big(\sigma^r_i - \sigma^t_i\big)C^{\mathrm{e}}_{ij}\big(\sigma^r_j - \sigma^t_j\big), \tag{10}$$

with respect to the return stress σ^r_i, where C^{e}_{ij} is the principal elastic compliance matrix. $(\cdot)^t$ and $(\cdot)^r$ denote quantities associated with the trial state and the return state respectively. The minimisation (10) is subject to the standard Kuhn-Tucker-Karush consistency conditions (6). Despite this process being referred to as a CPP, the return stress is not generally the closest point geometrically in standard stress space, but rather the stress that minimises the energy square norm (10).

In this paper we make use of energy-mapped ς_i space [10] to convert this CPP minimisation into a problem of finding the geometrically closest point on the yield envelope to a

trial point outside of the surface, where

$$\frac{1}{E}\varsigma_i\varsigma_i = \sigma_i C^{\mathrm{e}}_{ij}\sigma_j, \tag{11}$$

and E is the Young's modulus of the isotropic material. This allows us to find the geometric closest point (in ς_i space) through use of the following transformation

$$\varsigma_i = T_{ij}\sigma_j. \tag{12}$$

For isotropic linear elasticity, T_{ij} is solely a function of Poisson's ratio ν. Given the standard isotropic linear-elastic compliance matrix

$$C^{\mathrm{e}}_{ij} = \frac{1}{E}\Big(-\nu + \frac{1+\nu}{2}\delta_{ij}\Big) \tag{13}$$

the transformation tensor T_{ij} that can be used to convert between the stress spaces becomes

$$T_{ij} = \Big(\sqrt{1-2\nu} - \sqrt{1+\nu}\Big)/3 + \delta_{ij}\sqrt{1-\nu}. \tag{14}$$

This mapping leads to a squashing and a stretching of the yield surface in the hydrostatic and deviatoric directions respectively. The transformation is shown in Figure 1 for a spherical yield surface with $\nu = 0$, $\nu = 0.2$ and $\nu = 0.4$.

Once the closest point solution in energy-mapped stress space has been found, the solution can be transformed back to conventional stress space. For a NURBS yield surface we only need to map the control point locations, C_k, into energy-mapped space, the rest of the NURBS information remains unchanged. Also, we reduce the number of unknowns by one, replacing the return stress state σ^r_i with the local positions within the Knot vectors, ξ and η in (3) as the primary unknowns in the CPP problem.

3. Numerical implementation

In this paper we combine an initial coarse subdivision algorithm with a local Newton-Raphson approach to find the closest point on the NURBS surface to a trial stress state outside of the yield envelope. This is consistent with other approaches to finding the geometrically closest point to NURBS surfaces used in other fields [11, 12, 36, 41].

3.1. NURBS subdivision

The backward Euler (bE) search algorithm requires an initial starting point for the iterative process. For conventional plasticity models integrated using a bE approach, the starting point is taken to be the trial stress state outside of the yield envelope. However, in this paper the unknowns are the local positions ξ and η within the Knot vectors defining the surface. Therefore we need an initial estimate of the return ξ and η for a given trial

state outside of the yield envelope. The subdivision algorithm described in this section provides the, otherwise known, initial starting point for the iterative implicit bE stress integration process.

The following steps are taken to arrive at the starting point for the bE algorithm:

1. determine the unique Knot vector locations in the two local coordinates (ξ, η) and calculate the distance between the trial point and the Knot positions;
2. select the closest Knot (cK) location, (ξ_{cK}, η_{cK});
3. with $a = 1$ consider a new Knot interval

$$\xi \in \left[\frac{\xi_{cK-1} - \xi_{cK}}{2^a} + \xi_{cK} \ , \ \xi_{cK} + \frac{\xi_{cK+1} - \xi_{cK}}{2^a} \right] \qquad \text{and}$$
$$\eta \in \left[\frac{\eta_{cK-1} - \eta_{cK}}{2^a} + \eta_{cK} \ , \ \eta_{cK} + \frac{\eta_{cK+1} - \eta_{cK}}{2^a} \right];$$

4. grid the interval with the nine combinations of the centre of the interval (ξ_{cK}, η_{cK}) and its limits, then determine the distance between the trial point and the subdivided Knot positions; and
5. repeat steps 2 through 4 whilst incrementing $a = 1, 2, 3, \ldots, n_s$, where n_s is the number of subdivisions applied.

This process is shown in Figure 2 for a spherical yield surface with $\nu = 0$ so that conventional and energy-mapped stress space are equivalent. Figure 2 (i) shows the first subdivision step ($a = 1$), where the initially closest Knot location is at A and the closest subdivision position is at B (highlighted by the large grey shaded circle). The control point locations are shown by shaded circles and the grid for the first subdivision by black-shaded circles. The second subdivision is shown in Figure 2 (ii), in this case the previous closest point (B) remains the closest point to the trial location. The grid of subdivided points is shown by the white-shaded squares.

Figure 2 (iii) demonstrates the subdivision process in the local Knot coordinates for the first three subdivisions. After the first and second subdivisions the closest point is located at B and C, respectively. In the limit as $n_s \to \infty$ the subdivision closest point converges to the return stress state in energy-mapped stress space ($\varsigma_i^{cK} \to \varsigma_i^r$).

3.2. Stress integration algorithm

The output from the subdivision algorithm, (ξ_{cK}, η_{cK}), can be taken as the initial estimate for a Newton-Raphson process that is used to converge to a specified tolerance on the geometrically closest point on the yield surface (ς_i^r) to a trial location (ς_i^t) in energy-mapped stress space.

The unknowns in the implicit backward Euler stress integration process are the local positions on the NURBS surface

$$\{x\} = \{\xi \quad \eta\}^T. \tag{15}$$

Two corresponding residuals can be defined knowing that the return direction must be orthogonal to the tangent vectors of the NURBS surface

$$\{r\} = \left\{ (\varsigma_i^t - \varsigma_i^n)(S_{,\xi})_i \qquad (\varsigma_i^t - \varsigma_i^n)(S_{,\eta})_i \right\}^T. \tag{16}$$

where the tangent vectors, $(S_{,\xi})_i$ and $(S_{,\eta})_i$, are obtained by taking the derivatives of the NURBS surface with respect to the local coordinates (see [26] for efficient algorithms for computing these derivatives). Using these residuals we can apply a standard Newton process

$$\{\delta x\} = -\left[\frac{\partial r}{\partial x}\right]^{-1} \{r\} \qquad \text{and} \qquad \{x^n\} = \{x^{n-1}\} + \{\delta x\}, \tag{17}$$

where n is the Newton-Raphson iteration number with the initial condition that $\xi^0 = \xi_{cK}$ and $\eta^0 = \eta_{cK}$. The Hessian matrix in (17) is obtained by taking the derivative of the residuals with respect to the local Knot positions

$$\left[\frac{\partial r}{\partial x}\right] = \begin{bmatrix} -(S_{,\xi})_i(S_{,\xi})_i + (\varsigma_i^t - \varsigma_i^n)(S_{,\xi\xi})_i & -(S_{,\eta})_i(S_{,\xi})_i + (\varsigma_i^t - \varsigma_i^n)(S_{,\xi\eta})_i \\ -(S_{,\xi})_i(S_{,\eta})_i + (\varsigma_i^t - \varsigma_i^n)(S_{,\eta\xi})_i & -(S_{,\eta})_i(S_{,\eta})_i + (\varsigma_i^t - \varsigma_i^n)(S_{,\eta\eta})_i \end{bmatrix}, \tag{18}$$

again see [26] for efficient algorithms for computing these second-order derivatives. The Newton process continues until the L^2 norm of the residuals converge to a given tolerance.

A common problem in implicit stress integration is the stability of the algorithm due to the form of the yield function outside of the yield envelope [5]. Unless care is taken when specifying the yield equation it is possible to obtain a form that contains local minima, or even ancillary $f = 0$ loci in the inadmissible region of stress space. These undesirable features can *trap* the return path resulting in non-convergence, or more dangerously convergence to a spurious $f = 0$ surface outside of the intended yield envelope. These issues are removed in the this work as the iterative process starts and remains in the NURBS surface throughout the NR return algorithm providing a inherently stable process for smooth convex yield surfaces[2].

A Pseudo-code for the stress integration algorithm, covering both the subdivision algorithm and the Newton process, is given in Figure 4. The input for the algorithm is the trial location in energy mapped stress space along with the NURBS surface information, the function returns the closest point in energy mapped stress space. The tolerance on the NR process, `tol`, is typically set to 1×10^{-9}, the maximum number of NR iterations, `maxNRit`, to 10 and the number of subdivisions, n_s, to 5.

[2]Note that it is necessary to construct the NURBS surfaces from at least quadratic NURBS splines to ensure that the second derivatives of the surface exist. Care must also be taken at repeated Knot locations to ensure that the derivatives are finite (see Section 3.4)

3.3. Algorithmic consistent tangent

To achieve optimal convergence within a boundary value simulation it is essential to linearise the stress integration algorithm to form the algorithmic consistent tangent [32] (that is, the fourth order material stiffness tensor that is consistent with the stress-strain algorithm). This section provides that tangent following the approach of Clausen *et al.* [2–4]. The tangent is first constructed in principal stress space and then transformed into six-component stress space using the eigenvectors associated with the trial elastic strain state (see Appendix B for details).

The principal algorithmic consistent tangent for the stress integration algorithm given in this paper can be expressed as

$$D_{ij}^{alg} = D_{ij}^{c} - \frac{D_{ik}^{c}(S_{,\sigma})_k (S_{,\sigma})_l D_{lj}^{c}}{(S_{,\sigma})_a D_{ab}^{c} (S_{,\sigma})_b} \tag{19}$$

The modified elastic stiffness matrix is given by

$$D_{ij}^{c} = A_{ik} D_{kj}^{\mathrm{e}}, \tag{20}$$

where the modification matrix is given by

$$A_{ij} = \Big(\delta_{ij} + \Delta\gamma D_{ik}^{\mathrm{e}} (S_{,\sigma\sigma})_{kj}\Big)^{-1}. \tag{21}$$

The increment in the plastic multiplier can be obtained from

$$\Delta\gamma = \frac{||\Delta\sigma_i^{\mathrm{p}}||}{||D_{ij}^{\mathrm{e}} (S_{,\sigma})_j||}, \tag{22}$$

where $\Delta\sigma_i^{\mathrm{p}} = \sigma_i^t - \sigma_i^r$ is the plastic stress increment and $||\cdot||$ denotes the euclidean norm of the tensor.

The second derivative of the NURBS surface with respect to stress is

$$\begin{aligned} (S_{,\sigma\sigma})_{ij} \;=\; & \Big(\epsilon_{ikl}(S_{,\eta})_k (S_{,\xi\xi})_l + \epsilon_{ikl}(S_{,\eta\xi})_k (S_{,\xi})_l\Big)(\xi_{,\sigma})_j + \\ & \Big(\epsilon_{ikl}(S_{,\eta})_k (S_{,\xi\eta})_l + \epsilon_{ikl}(S_{,\eta\eta})_k (S_{,\xi})_l\Big)(\eta_{,\sigma})_j, \end{aligned} \tag{23}$$

where derivatives of the local Knot coordinates with respect to stress can be obtained from the inversion of the Jacobian matrix linking the local NURBS coordinates with the principal stress directions

$$[J] = \left[\frac{\partial\sigma}{\partial\xi}\right] = \Big[(S_{,\xi})_i \quad (S_{,\eta})_i \quad (S_{,\sigma})_i\Big]. \tag{24}$$

The normal to the NURBS surface, $(S_{,\sigma})_i$ provides the third direction, orthogonal to the

tangent vectors, in the transformation.

3.3.1. Six-component stress space

The plasticity model presented in this paper has been expressed in principal components. It is therefore necessary to detail the mapping between of this model into generalised 6-component space. The equations to convert the stress and strain measures into 6-component space are given in Appendix B, the appendix also details the transformation of the algorithmic (or elasto-plastic) stiffness matrix. However, before this can be achieved it is necessary to specify the shear components of the algorithmic stiffness matrix. For convenience we switch to matrix notation in this section.

The shear terms of the modified elastic stiffness matrix are given by

$$[D_G^c] = [A_G][D_G^e], \tag{25}$$

where $[D_G^e]$ is a three-by-three matrix containing the shear components of the elastic stiffness matrix, the modification matrix for the shear components is given by [4]

$$[A_G] = \begin{bmatrix} 1 + \frac{\Delta\sigma_1^p - \Delta\sigma_2^p}{\sigma_1^r - \sigma_2^r} & 0 & 0 \\ 0 & 1 + \frac{\Delta\sigma_1^p - \Delta\sigma_3^p}{\sigma_1^r - \sigma_3^r} & 0 \\ 0 & 0 & 1 + \frac{\Delta\sigma_2^p - \Delta\sigma_3^p}{\sigma_2^r - \sigma_3^r} \end{bmatrix}. \tag{26}$$

The stiffness matrix used in (B.1) is therefore

$$[D] = \begin{bmatrix} [D^{alg}] & [0] \\ [0] & [D_G^c] \end{bmatrix}, \tag{27}$$

where [0] is a three-by-three matrix full of zeros and $[D^{alg}]$ is the principal elastic stiffness matrix from (19).

The full NURBS plasticity constitutive approach is summarised using the pseudo-code given in Figure 5.

3.4. Corners

Several classical yield surfaces are only C^0 continuous and contain sharp corners, Tresca and Mohr-Coulomb are two such examples. However, the algorithm presented in this paper is limited to smooth convex surfaces where the second derivative is defined. It is therefore necessary to introduce local rounding to any corners or apexes.

Consider the following open Knot vector that interpolates between five control points (as shown in Figure 3(i)), where

$$\Xi = \{0, 0, 0, 1, 1, 2, 2, 2\} \quad \text{and} \quad w = \{1, 1, 1, 1, 1\}. \tag{28}$$

At $\xi = 1$ the NURBS curve is geometrically only C^0 continuous. One solution that removes the point on the line when the normal is undefined is to introduce two additional control points and an additional interval in the Knot vector. This allows the corner to be rounded using a circular arc tangent to the two segments. For the case shown in Figure 3 (ii) the Knot vector and weights are

$$\Xi = \{0, 0, 0, 1, 1, 2, 2, 3, 3, 3\} \quad \text{and} \quad w = \{1, 1, 1, \cos(\phi/2), 1, 1, 1\}. \tag{29}$$

The weight of the *corner* control point is only dependent on the internal angle between the two straight segments. The position of the additional control points can be specified as some portion, α, of the distance between the corner control point and its neighbour, l, as shown in Figure 3. Rounding of apexes on NURBS surfaces can be achieved by simply rounding the compounded NURBS curves. The consequence of this local round on stress integration accuracy is explored in Section 4.1.

4. Numerical simulations

This section presented numerical simulations using the NURBS plasticity framework. In all of the analyses the tolerance on the NR process, `tol`, was set to 1×10^{-9}, the maximum number of NR iterations, `maxNRit`, to 10 and the number of subdivisions, n_s, to 5.

4.1. Stress return error analysis

This section presents stress return error analyses for two yield envelopes represented using NURBS, namely the cylindrical von Mises yield surface and the prismatic hexagonal yield surface of Tresca.

4.1.1. von Mises plasticity

The perfect plasticity von Mises yield envelope combined with linear isotropic elasticity serves as a useful benchmark due to the availability of an exact stress integration algorithm [19]. The NURBS Knot vector and weights for the von Mises yield surface are provided in Appendix A.1. The yield envelope for the model can be defined as

$$f = \rho - \rho_y = 0, \tag{30}$$

where the deviatoric stress is $\rho = \sqrt{2J_2}$ with $J_2 = \frac{1}{2}s_{ij}s_{ji}$ and $s_{ij} = \sigma_{ij} - \frac{1}{3}\sigma_{kk}\delta_{ij}$, ρ_y is the yield stress of the material and defines the radius of the von Mises cylinder. Here the yield stress was taken to be $\rho_y = 1$MPa, the Young's modulus was $E = 100$MPa and the Poisson's ratio was $\nu = 0.2$.

The stress integration errors for a von Mises yield surface using the NURBS integration procedure described in Section 2.2 are shown in Figure 6. The stress state is initially located on the shear meridian in the $\sigma_{zz} > \sigma_{yy} > \sigma_{xx}$ sextant of stress space. This point is then

subjected to a stress increment that will take the trial stress state outside of the yield envelope into one of the three sextants shown in Figure 6. The space of trial states was explored for $\rho_t/\rho_y \in [1, 6]$ and the errors associated with the trial state shown on the right of Figure 6. The normalised error measure used is

$$\text{error} = \frac{||\{\sigma_{\text{NURBS}}\} - \{\sigma_e\}||}{||\sigma_e||}, \tag{31}$$

where $\{\sigma_{\text{NURBS}}\}$ is the stress return location associated with the NURBS model and $\{\sigma_e\}$ is the exact stress return [19].

Although errors of over 20% are present in the model, exactly the same level of errors are observed in the von Mises yield surface integrated with a conventional bE stress integration procedure. As expected with any predictor-correction stress integration algorithm, the error increases as the tangential proportion of the stress increment increases.

4.1.2. Tresca corner rounding

Here we investigate the consequence of rounding on the errors in the stress integration algorithm for the Tresca yield envelope. The normalised error measure (31) is used but the *exact* return stress is determined from a conventional bE implementation of the model based on the work of Clausen *et al.* [4]. Due to the planar nature of the Tresca yield surface, the updated stress from the bE algorithm will be exact provided that the stress increment should not cause the return stress state to cross between sextants of stress space. The Tresca yield surface can be defined as

$$f = \sigma_1 - \sigma_3 - \sigma_y = 0, \tag{32}$$

where σ_y is the yield stress of the material. Here the yield stress was taken to be $\sigma_y = 1$MPa, the Young's modulus was $E = 100$MPa and the Poisson's ratio was $\nu = 0.2$.

The maximum error for any trial location is given in Table 1 for different values of rounding parameter, in this case the space of trial states was explored for $\theta_t \in [-\pi/6, \pi/6]$ with $\rho_t/\sigma_y = 1.5$ as the maximum error does not depend on the radial distance from the surface. The maximum errors are located along a ray tangent to the true Tresca surface at the compression or tension meridians (as shown on the right of Figure 7). These points should return to the compression/extension meridian but instead they return to a point on the rounded surface. The maximum error is this case is αl, where for this yield surface $l = \sigma_y/2$, therefore the maximum normalised error from (31) is $\alpha/2$. This is verified in Table 1 showing that the error converges linearly with the rounding parameter and for $\alpha = 1 \times 10^{-5}$ the maximum error is 4.99×10^{-6}.

The variation of the error with trial Lode angle, θ_t, is shown in Figure 7 where the stress return error has been normalised with respect to the maximum error (as given in

Table 1). The Lode angle, θ, is defined as

$$\theta = \frac{1}{3}\arcsin\left(\frac{-3\sqrt{3}}{2}\frac{J_3}{J_2^{3/2}}\right) \quad \in \big[-\pi/6, \pi/6\big], \tag{33}$$

where $J_3 = \frac{1}{3}s_{ij}s_{jk}s_{ki}$. The distribution of this normalised error is the same for all of the explored α values.

For trial points located on the compression or extension meridians ($\theta_t = \pm\pi/6$) the error is

$$\text{corner error} = \frac{\alpha l(1-\cos(\phi/2))}{\sin(\phi/2)},$$

where ϕ is the internal angle of the rounded corner (see Figure 3) and for the Tresca yield surface $\phi = \pi/3$. Therefore the maximum normalised error from (31) is $\alpha(1-\sqrt{3}/2)$, that is 26.8% of the maximum error, $\alpha/2$. This is verified by the solid black line on Figure 7.

The number of Newton-Raphson iterations (NRit) for the different trial states is also shown by the grey dashed line in Figure 7 and the maximum number of NRits for any trial state given in Table 1 demonstrating the robustness of the algorithm with different α.

4.2. Notched plate

Here we present the analysis of the plane strain stretching of a double-notched plate. The problem was initially presented by Nagtegaal *et al.* [23] for small strain plasticity to demonstrate the spurious response of standard finite elements and was subsequently re-analysed in a number of papers [28, 31, 33]. The plate had a Young's modulus of 206.9GPa, Poisson's ratio of 0.29 and was modelled using an elastic-perfectly plastic Prandtl-Reuss constitutive model with yield stress of $\rho_y = 0.45$GPa. Nagtegaal *et al.* [23] provided the small strain analytical limit load, controlled by the stress at the notch $\sigma_{\lim} \approx 2.97\rho_y$. The specimen had a total height and width of 30mm and 10mm respectively, with a 2mm unit linking ligament at mid height. For this geometry the small strain limit load is $f^{\lim} \approx 2.673$kN. Due to symmetry, only one quarter of the specimen was initially discretised using 75 plane strain eight-noded elements with reduced four-point integration, as shown in Figure 8. A displacement of 0.2mm was applied in 20 equal displacement-controlled increments.

The problem was analysed using both the NURBS implementation of the von Mises yield surface and the exact implementation of Prandtl-Reuss plasticity of Wei *et al.* [38][3]. The load versus displacement response of the two models is nearly identical (as shown in Figure 8) and both the models converge to the analytical solution with mesh refinement.

[3]Note that although Wei *et al.* [38] were not the first to provide an exact stress return for the Prandtl-Reuss model, that was provided by Krieg and Krieg [19], they were the first to provide the consistent linearisation of the model allowing for optimum convergence of the global out-of-balance force therefore their formulation is used here.

Three different error measures are give in Table 3 for the three different discretisations. Two are errors associated with the final limit load

$$e_{(\cdot)} = \frac{|f^{\lim}_{NURBS} - f^{\lim}_{(\cdot)}|}{|f^{\lim}_{(\cdot)}|}, \tag{34}$$

where the subscripts $_a$ and $_e$ relate to the analytical limit load of $f^{\lim}_a \approx 2.673$kN and the limit load obtained through the exact implementation of the von Mises yield surface $f^{\lim}_e$, respectively. The final error, e_σ, is the average of the normalised error between the NURBS stress states at the Gauss points and that of of the exact implementation of the von Mises model. Linear convergence is observed in the analytical limit load error whereas the other two errors remain relatively stable with mesh refinement.

Table 2 provides the out-of-balance force values during the global Newton Raphson (NR) process for loadsteps 5 through 8 for the NURBS model. It can be observed that the model approaches optimum (2nd order) convergence of the global Newton process, validating the derivation an implementation of the algorithmic consistent tangent.

4.3. Rigid footing

This section presents the analysis of a smooth rigid strip footing under plane strain. The footing was 1m wide and was subjected to a vertical displacement of 50mm over 50 loadsteps. Due to symmetry only half of the 10m by 5m domain was discretised using 135 eight-noded quadrilateral finite elements with reduced four-point integration (as shown on the right of Figure 9). The mesh used is that same as that adopted by [34] and [7]. The material was assumed to be weightless and had a Young's modulus of $E = 100$MPa and a Poisson's ratio of $\nu = 0.3$. The yielding of the material was governed by a Tresca yield surface (32), where the yield stress was taken as $\sigma_y = 200$kPa, represented by a NURBS surface with locally rounded corners where the rounding parameter was set to $\alpha = 1 \times 10^{-5}$.

The normalised pressure versus displacement response is shown in Figure 9 for both the NURBS yield surface (black-dashed line) and for a conventional backward Euler implementation of the model (thick grey line) based on the work of Clausen *et al.* [4]. The results are indistinguishable with both simulations having an error of 0.8% compared to the analytical limit of

$$2p/\sigma_y = 2 + \pi,$$

where p is the average pressure under the footing. This demonstrates the ability of the local rounding to reproduce the boundary values simulation results of the geometrically exact yield envelope.

5. Conclusions

This paper has presented for the first time a NURBS-based plasticity framework that allows for any smooth convex isotropic perfect-plasticity yield surface to be described and

implemented using the same numerical algorithm. To use different yield envelopes only the control point and NURBS information changes. The numerical integration technique combines an initial coarse searching algorithm with a Newton-Raphson process to solve for the local position within the NURBS Knot vectors. The method is inherently stable as, unlike conventional predictor-corrector algorithms, the return stress state remains in the yield surface during the iterative process.

The framework has been validated for two plasticity models with von Mises and Tresca yield envelopes. In the case of von Mises plasticity the NURBS approach was compared with an exact implementation [19, 38] demonstrating that the errors in the process are the same as that on a convectional bE method and that for a boundary value simulation the model has excellent agreement with the exact implementation. Asymptotic quadratic convergence of the global out-of-balance force has also been demonstrated validating the algorithmic consistent tangent. For the Tresca implementation local rounding has been introduced into the model to avoid the difficulties of dealing with sharp corners in the Newton process. However, the maximum error due to this local rounding converges linearly with the rounding length and the method is stable over a wide range of rounding parameters. Provided a small rounding parameter is adopted the errors are insignificant compared with the standard stress integration errors. The Tresca implementation was also validated in a boundary value simulation of a rigid footing bearing onto a weightless soil with results indistinguishable from a conventional Tresca implementation with sharp corners.

This paper has focused on perfect plasticity yield envelopes. It would be possible to extend the framework to include hardening/softening plasticity however, any implemented hardening laws would have to be reformulated in terms of the movement of the control points.

References

[1] A. Anandarajah, Computational methods in Elasticity and Plasticity: Solids and Porus Media, Springer, 2010.

[2] J. Clausen, L. Damkilde, International Journal of Rock Mechanics & Mining Sciences 45 (2008) 831–847.

[3] J. Clausen, L. Damkilde, L. Andersen, Efficient return algorithms for associated plasticity with multiple yield planes, Int. J. Numer. Meth. Engng 66 (2006) 1036–1059.

[4] J. Clausen, L. Damkilde, L. Andersen, An efficient return algorithm for non-associated plasticity with linear yield criteria in principal stress space, Computers & Structures 85 (2007) 1795–1807.

[5] W.M. Coombs, R.S. Crouch, Algorithmic issues for three-invariant hyperplastic critical state models, Comput. Methods Appl. Mech. Engrg. 200 (2011) 2297–2318.

[6] W.M. Coombs, R.S. Crouch, Non-associated reuleaux plasticity: analytical stress integration and consistent tangent for finite deformation mechanics, Comput. Methods Appl. Mech. Engrg. 200 (2011) 1021–1037.

[7] W.M. Coombs, R.S. Crouch, C.E. Augarde, Reuleaux plasticity: analytical backward Euler stress integration and consistent tangent, Comput. Methods Appl. Mech. Engrg. 199 (2010) 1733–1743.

[8] J.A. Cottrell, T.J.R. Hughes, Y. Bazilevs, Isogeometric Analysis: Toward Integration of CAD and FEA, Wiley, New York, 2009.

[9] M. Crisfield, Non-linear Finite Element Analysis of Solids and Structures. Volume 1: Essentials, John Wiley & Sons Ltd, 1991.

[10] R. Crouch, H. Askes, T. Li, Analytical CPP in energy-mapped stress space: application to a modified Drucker-Prager yield surface, Comput. Methods Appl. Mech. Engrg. 198 (2009) 853–859.

[11] E. Dyllong, W. Luther, Distance calculation between a point and a NURBS surface, in: Int. Conf. on Curves & Surfaces, volume Vol. 1: Curve & Surface Design, Saint-Malo, France.

[12] E.G. Gilbert, C.P. Foo, Computing the distance between general convex objects in three-dimensional space, IEEE Transactions on Robotics and Automation 6 (1990) 53–61.

[13] A.A. Ilyushin, Some problems in the theory of plastic deformation, Prikl. Mat. Mekh. (1943) 245–272.

[14] M. Kojić, The governing parameter method for implicit integration of viscoplastic constitutive relations for isotropic and orthotropic metals, Computational Mechanics 19 (1996) 49–57.

[15] M. Kojić, Stress integration procedures for inelastic material models within the finite element method, Appl. Mech. Rev. 55 (2002) 389–414.

[16] M. Kojić, K. Bathe, Inelastic Analysis of Solids and Structures, Springer Berlin Heidelberg New York, 2005.

[17] A. Kossa, L. Szabó, Exact integration of the von Mises elastoplasticity model with combined linear isotropic-kinematic hardening., International Journal of Plasticity 25 (2009) 1083–1106.

[18] A. Kossa, L. Szabó, Numerical implementation of a novel accurate stress integration scheme of the von Mises elastoplasticity model with combined linear hardening, Finite Elements in Analysis and Design 46 (2010) 391–400.

[19] R. Krieg, D. Krieg, Accuracies of numerical solution methods for the elastic-perfectly plastic model, Journal of Pressure Vessel Technology 99 (1977) 510–515.

[20] B. Loret, J. Prévost, Accurate numerical solutions for Drucker-Prager elastic plastic models, Comput. Methods Appl. Mech. Engrg. 54 (1986) 259–277.

[21] A. Mendelson, Plasticity: theory and application, The Macmillan Co., NY, 1968.

[22] J. Nagtegaal, On the implementation of inelastic constitutive equations with special reference to large deformation problems, Comput. Methods Appl. Mech. Eng. 33 (1982) 469–484.

[23] J. Nagtegaal, D. Parks, J. Rice, On numerically accurate finite element solutions in the fully plastic range, Comp. Methods Appl. Mech. Engng. 4 (1974) 153–177.

[24] G. Nayak, O. Zienkewicz, Elasto-plastic stress analysis. a generalization for various constitutive relations including strain softening, Int. J. Numer. Meth. Eng. 5 (1972) 113–135.

[25] M. Ortiz, E. Popov, Accuracy and stability of integration algorithms for elastoplastic constitutive relations, Int. J. Numer. Meth. Eng. 21 (1985) 1561–1576.

[26] L. Piegl, W. Tiller, The NURBS book, Springer Science & Business Media, 2012.

[27] M. Safaei, M.G. Lee, W.D. Waele, Evaluation of stress integration algorithms for elastic-plastic constitutive models based on associated and non-associated flow rules, Comput. Meth. Appl. Mech. Engrg. 295 (2015) 414–445.

[28] J.C. Simo, Associative coupled thermoplasticity at finite strains: Formulation, numerical analysis and implementation, Comput. Methods Appl. Mech. Eng. 98 (1992) 41–104.

[29] J.C. Simo, T.J.R. Hughes, Computational inelasticity, Springer, New York, 1998.

[30] J.C. Simo, M. Ortiz, A unified approach to finite deformation elastoplastic analysis based on the use of hyperelastic constitutive equations, Comput. Methods Appl. Mech. Engrg. 49 (1985) 221 – 245.

[31] J.C. Simo, M.S. Rifai, A class of mised assumed strain methods and the method of incompatible modes, Int. J. Num. Meth. Engng. 29 (1990) 1595–1638.

[32] J.C. Simo, R.L. Taylor, Consistent tangent operators for rate-independent elastoplasticity, Comput. Methods Appl. Mech. Eng. 48 (1985) 101–118.

[33] E.A. de Souza Neto, D. Perić, M. Dutko, D.R.J. Owen, Design of simple low order finite elements for large strain analysis of nearly incompressible solids, Int. J. Solids Structures 33 (1996) 3277–3296.

[34] E.A. de Souza Neto, D. Perić, D.R.J. Owen, Computational methods for plasticity: Theory and applications, John Wiley & Sons Ltd, 2008.

[35] L. Szabó, A semi-analytical integration method for J2 flow theory of plasticity with linear isotropic hardening, Comput. Meth. Appl. Mech. Engrg. 198 (2009) 2151–2166.

[36] C. Turnbull, S. Cameron, Computing distances between NURBS-defined convex objects, in: Robotics and Automation, 1998. Proceedings. 1998 IEEE International Conference on, volume 4, pp. 3685–3690.

[37] M. Vrh, M. Halilovič, B. Štok, Improved explicit integration in plasticity, Int. J. Numer. Meth. Engng. 81 (2010) 910–938.

[38] Z. Wei, D. Perić, D.R.J. Owen, Consistent linearization for the exact stress update of Prandtl-Reuss non-hardening elastoplastic models, Int. J. Num. Meth. Engng. 39 (1996) 1219–1235.

[39] M. Wilkins, Calculation of elastic-plastic flow, in: S. Fernback, M. Rotenberg (Eds.), Methods of Computational Physics, volume 3, Academic Press, New York, 1964.

[40] M.h. Yu, Advances in strength theories for materials under complex stress state in the 20th century, Appl Mech Rev 55 (2002) 169–218.

[41] J. Zhou, E.C. Sherbrooke, N.M. Patrikalakis, Computation of stationary points of distance functions, Engineering with Computers 9 (1993) 231–246.

rounding parameter, α	1×10^{-1}	1×10^{-2}	1×10^{-3}	1×10^{-4}	1×10^{-5}
max. error	4.31×10^{-2}	4.91×10^{-3}	4.98×10^{-4}	4.99×10^{-5}	4.99×10^{-6}
max. NRit	4	3	3	3	3

Table 1: Variation with maximum error with rounding parameter, α, for the Tresca yield surface.

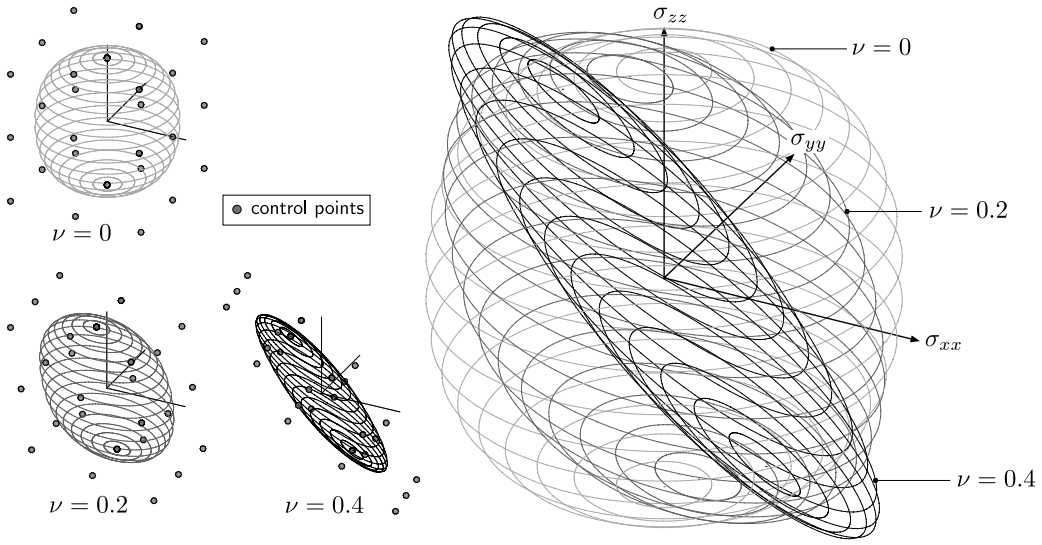

Figure 1: energy-mapped stress space transformation for a spherical yield surface.

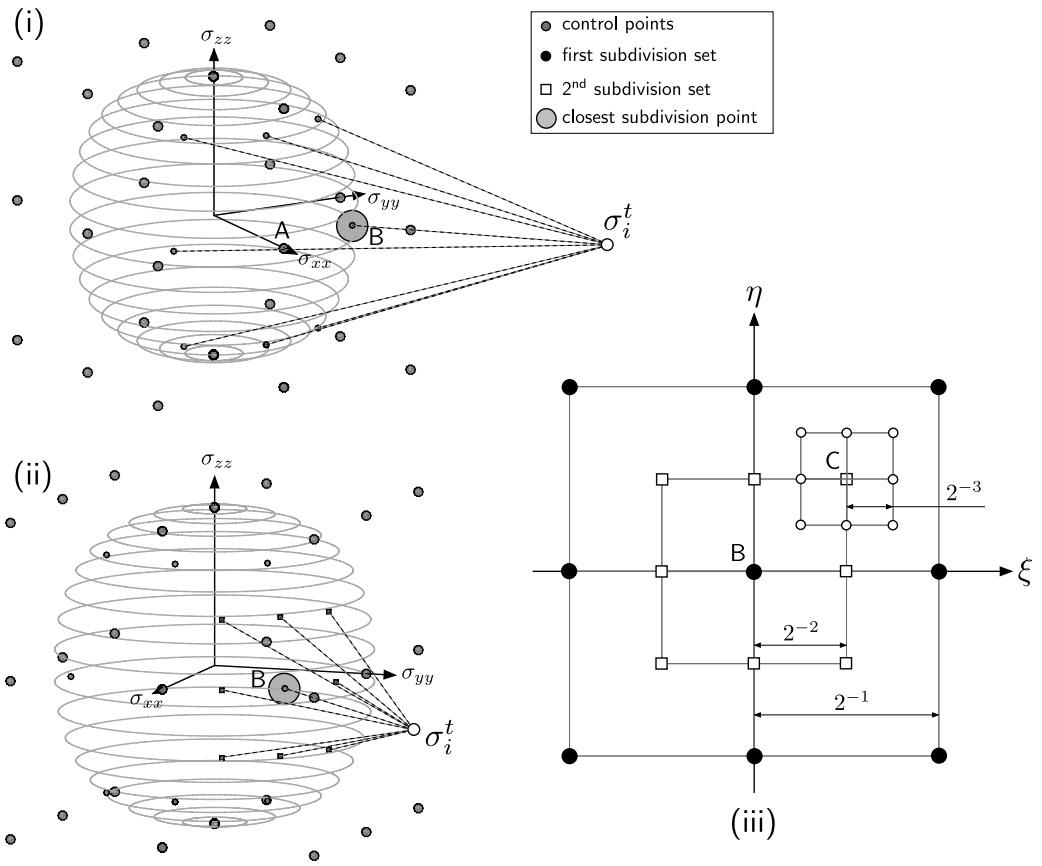

Figure 2: subdivision algorithm for a spherical yield surface (where Knot positions are integers) with $\nu = 0$: (i) first subdivision step, (ii) second subdivision and (iii) the subdivision process in the local Knot vector coordinates.

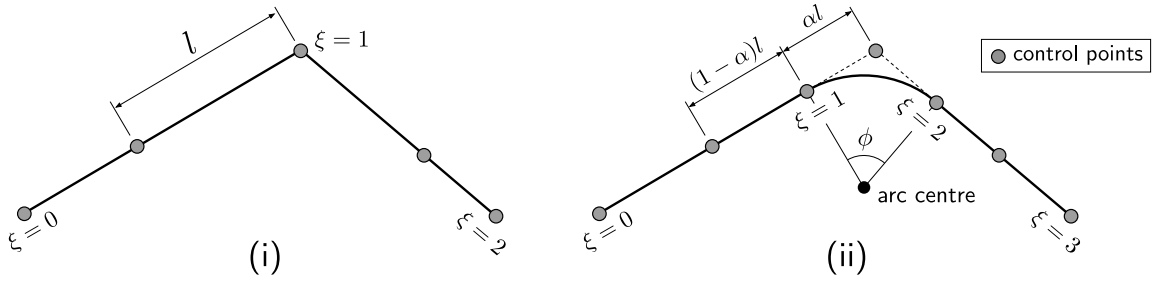

Figure 3: NURBS corner rounding.

1. INPUT: $\{\varsigma^t\}$, n_s & NURBS information (Ξ, ${}^{\varsigma}C$, w, p).

   (a) NURBS surface subdivision

      i. determine the distance between $\{\varsigma^t\}$ and the Knot locations on the NURBS surface;
      ii. select the Knot location with the minimum distance, $\{\xi_{cK}\}$;
      iii. FOR $a = 1 : n_s$ *(number of subdivision steps)*
         - determine the local coordinate limits of the local search region;
         - determine the distance between $\{\varsigma^t\}$ and the eight subdivided Knot locations;
         - select the Knot location with the minimum distance (ξ_{cK}, η_{cK})
      iv. END FOR

   (b) backward Euler stress return algorithm using N-R

      i. take $\{\xi_{cK}\}$ as the initial estimate for the Knot location in the N-R process;
      ii. initial error, set $||\{r\}|| = 2 \times$ `tol`
      iii. WHILE ($||\{r\}|| >$ `tol`) && (`NRit` < `maxNRit`)
         - determine the first and second derivatives of the NURBS surface;
         - calculate the residuals, $\{r\}$, (16);
         - form the Hessian matrix, $[\partial r/\partial x]$, (18);
         - determine the increment in the unknowns, $\{\delta x\}$, and update $\{x\}$ (17);
      iv. END WHILE

2. OUTPUT: closest point on the NURBS surface, $\{\varsigma_{cp}\}$

Figure 4: Pseudo-code for the NURBS stress return (the tolerance, `tol`, is typically set to 1×10^{-9}).

	loadstep			
NR iteration	5	6	7	8
1	6.581×10^{-2}	5.089×10^{-2}	2.721×10^{-2}	3.582×10^{-2}
2	8.132×10^{-3}	1.253×10^{-3}	3.581×10^{-3}	3.947×10^{-4}
3	4.182×10^{-6}	1.397×10^{-6}	1.294×10^{-5}	1.554×10^{-7}
4	7.588×10^{-11}	2.143×10^{-12}	4.668×10^{-10}	1.419×10^{-13}

Table 2: Notched plate convergence for the NURBS implementation of the von Mises yield surface.

1. INPUT: $\{\varepsilon^t\}$, E, ν & NURBS information (Ξ, C, w, p).

   (a) Transform the trial elastic strain, $\{\varepsilon^t\}$, into its principal components and store the associated eigenvectors.

   (b) Calculate the principal (elastic) trial stress, $\{\sigma^t\} = [D^{\mathrm{e}}]\{\varepsilon^t\}$.

   (c) Transform the trial stress, $\{\sigma^t\}$, and the control point locations, $[C^p]$, to energy mapped stress space.

   (d) Determine the closest point between the trial stress state, $\{\varsigma^t\}$, and the NURBS surface in energy mapped stress space (refer to the algorithm in Figure 4)

   (e) Determine the value of the yield function at the based on the closest point and the trial state (3).

   (f) IF $f >$ tol (*elasto-plastic behaviour*)

      i. transform the return stress state, $\{\varsigma_{cp}\}$, back to conventional stress space;
      ii. calculate the updated elastic strain, $\{\varepsilon^{\mathrm{e}}_{n+1}\} = [C^{\mathrm{e}}]\{\sigma_{n+1}\}$;
      iii. determine the algorithmic consistent tangent matrix, $[D^{a\,\mathrm{lg}}]$;

   (g) ELSE (*elastic behaviour*)

      i. updated stress equal to the trial stress, $\{\sigma_{n+1}\} = \{\sigma^t\}$;
      ii. updated elastic strain equal to the trial strain, $\{\varepsilon^{\mathrm{e}}_{n+1}\} = \{\varepsilon^t\}$; and
      iii. algorithmic tangent equal to the elastic tangent, $[D^{alg}] = [D^{\mathrm{e}}]$.

   (h) END IF

   (i) Transform the principal components back to generalised space using the eigenvectors stored at step (a).

2. OUTPUT: $\{\sigma_{n+1}\}$, $\{\varepsilon_{n+1}\}$ and $[D^{alg}]$

Figure 5: Pseudo-code for the NURBS constitutive model.

element size (mm)	load error, e_e	load error, e_a	stress error, e_σ
1.00×10^{-3}	8.65×10^{-5}	1.25×10^{-1}	3.24×10^{-3}
0.50×10^{-3}	6.32×10^{-5}	6.59×10^{-2}	3.22×10^{-3}
0.25×10^{-3}	4.71×10^{-5}	3.35×10^{-2}	3.02×10^{-3}

Table 3: Notched plate errors for the NURBS implementation of the von Mises yield surface.

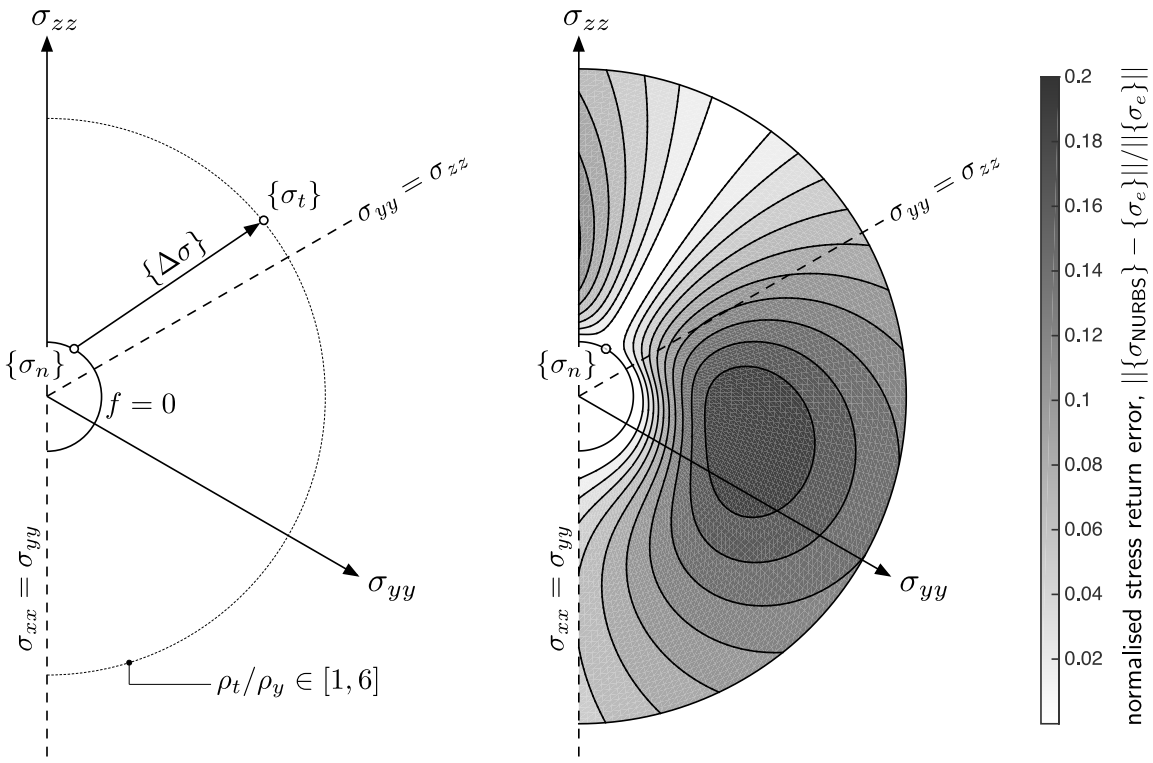

Figure 6: Stress return error analysis for a von Mises NURBS yield envelope.

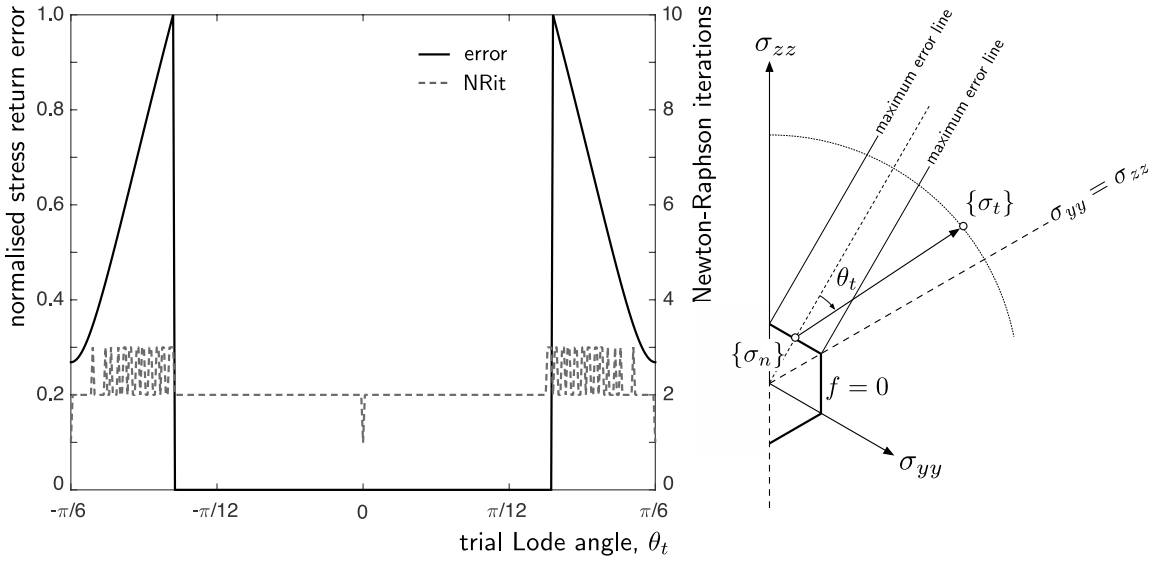

Figure 7: Stress return error analysis for a Tresca NURBS yield envelope for $\alpha = 1 \times 10^{-5}$.

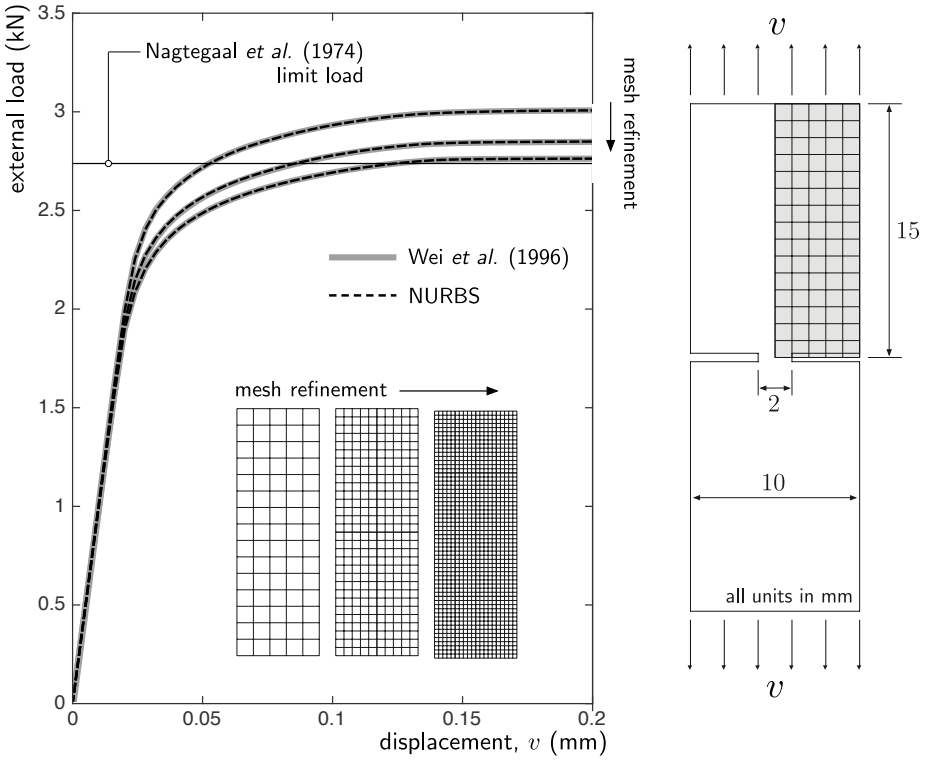

Figure 8: Notched plate load versus displacement comparison of the NURBS implementation of the von Mises yield surface with the exact implementation of Wei *et al.* [38] for three different discretisations.

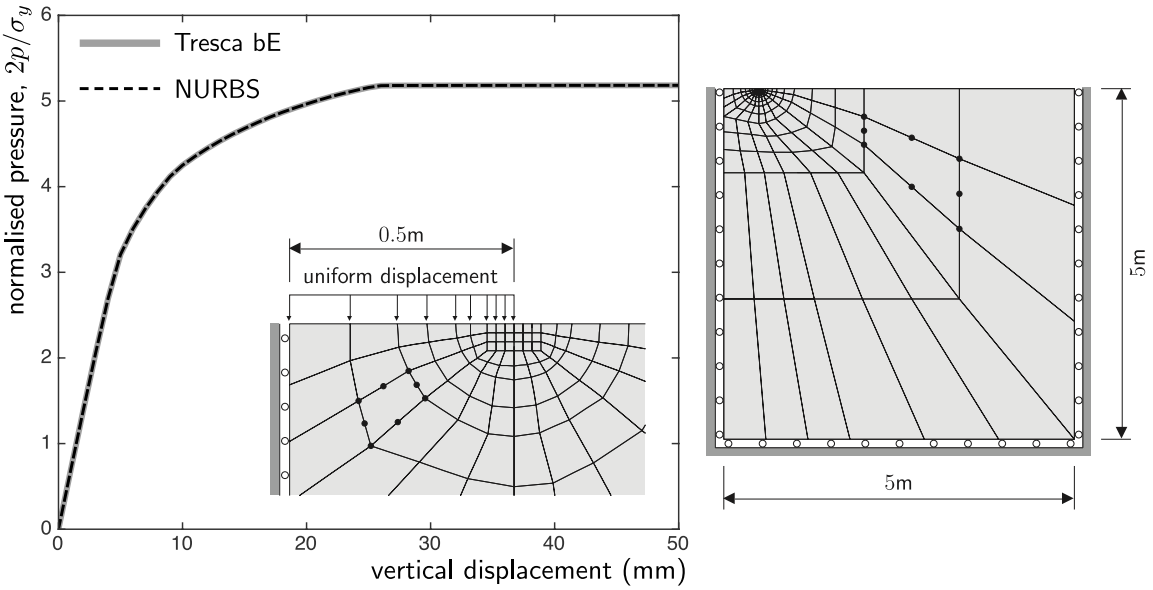

Figure 9: Normalised pressure versus displacement response and finite element descretisation of a rigid footing bearing onto a weightless soil.

Appendix A. Knot vectors

Appendix A.1. von Mises yield surface

The Knot vectors for a second-order ($p = 2$) von Mises yield surface are

$$\Xi = \{0, 0, 0, 1, 1, 2, 2, 3, 3, 4, 4, 4\} \qquad \text{and} \qquad \Lambda = \{0, 0, 0, 1, 1, 1\} \tag{A.1}$$

and the weights are given by

$$w_i = \{1, \frac{1}{\sqrt{2}}, 1, \frac{1}{\sqrt{2}}, 1, \frac{1}{\sqrt{2}}, 1, \frac{1}{\sqrt{2}}, 1\} \qquad \text{and} \qquad w_j = \{1, 1, 1\}. \tag{A.2}$$

The control points are located at

$$\{C\}_{i,j} = \frac{(I_1)_j}{3} + \sqrt{2/3}\rho_i \Big\{ \sin(\theta_i - 2\pi/3) \quad \sin(\theta_i) \quad \sin(\theta_i + 2\pi/3) \Big\}^T \tag{A.3}$$

where

$$\rho = \rho_y \Big\{ 1 \quad \sqrt{2} \quad 1 \quad \sqrt{2} \quad 1 \quad \sqrt{2} \quad 1 \quad \sqrt{2} \quad 1 \Big\}^T, \tag{A.4}$$

$$\theta = \pi/12 \Big\{ -2 \quad 1 \quad 4 \quad 10 \quad 13 \quad 16 \quad 19 \quad 22 \Big\}^T, \qquad I_1 = \beta\rho_y \Big\{ -1 \quad 0 \quad 1 \Big\}^T \tag{A.5}$$

and β is a large constant that extends the surface sufficiently in the hydrostatic direction to cover all possible return states.

Appendix B. Stress transformation

The following relations can be used to transform between six-component and principal stress and strain space

$$\{\hat{\sigma}\} = [Q]^T \begin{Bmatrix} \{\sigma\} \\ \{0\} \end{Bmatrix}, \qquad \{\hat{\varepsilon}\} = [Q]^{-1} \begin{Bmatrix} \{\varepsilon\} \\ \{0\} \end{Bmatrix} \qquad \text{and} \qquad [\hat{D}] = [Q]^T [D][Q], \tag{B.1}$$

where $\hat{(\cdot)}$ denotes the six-component stress and strain quantities. The transformation matrix is given by

$$[Q] = \begin{bmatrix} (q_1)^2 & (q_2)^2 & (q_3)^2 & q_1 q_2 & q_2 q_3 & q_3 q_1 \\ (q_4)^2 & (q_5)^2 & (q_6)^2 & q_4 q_5 & q_5 q_6 & q_6 q_4 \\ (q_7)^2 & (q_8)^2 & (q_9)^2 & q_7 q_8 & q_8 q_9 & q_9 q_7 \\ 2q_1 q_4 & 2q_2 q_5 & 2q_3 q_6 & q_1 q_5 + q_4 q_2 & q_2 q_6 + q_5 q_3 & q_3 q_4 + q_6 q_1 \\ 2q_4 q_7 & 2q_5 q_8 & 2q_6 q_9 & q_4 q_8 + q_7 q_5 & q_5 q_9 + q_8 q_6 & q_6 q_7 + q_9 q_4 \\ 2q_7 q_1 & 2q_8 q_2 & 2q_9 q_3 & q_7 q_2 + q_1 q_8 & q_8 q_3 + q_2 q_9 & q_9 q_1 + q_3 q_7 \end{bmatrix}, \tag{B.2}$$

where the components q_i are associated with the trial elastic strain eigenvectors

$$[q] = \begin{bmatrix} q_1 & q_4 & q_7 \\ q_2 & q_5 & q_8 \\ q_3 & q_6 & q_9 \end{bmatrix}. \tag{B.3}$$